Mon. Not. R. Astron. Soc. **000**, 000–000 (0000) Printed 21 August 2023 (MN LaTeX style file v2.2)

Magnetic fields of low-mass main sequences stars: Nonlinear dynamo theory and mean-field numerical simulations

N. Kleeorin,[1,2] I. Rogachevskii,[1,3] N. Safiullin,[4] R. Gershberg,[5] S. Porshnev[4,6]
[1] *Department of Mechanical Engineering, Ben-Gurion University of Negev, POB 653, 84105 Beer-Sheva, Israel*
[2] *Institute of Continuous Media Mechanics, Korolyov str. 1, Perm 614013, Russia*
[3] *Nordita, KTH Royal Institute of Technology and Stockholm University, Roslagstullsbacken 23, SE-10691 Stockholm, Sweden*
[4] *Department of Radio Electronic and Informational Technology, Ural Federal University, 19 Mira str., 620002 Ekaterinburg, Russia*
[5] *Crimean Astrophysical Observatory, RAN, Nauchny, Russia*
[6] *N.N. Krasovskii Institute of Mathematics and Mechanics (IMM UB RAS), Ekaterinburg, Russia*

21 August 2023

ABSTRACT

Our theoretical and numerical analysis have suggested that for low-mass main sequences stars (of the spectral classes from M5 to G0) rotating much faster than the sun, the generated large-scale magnetic field is caused by the mean-field $\alpha^2\Omega$ dynamo, whereby the α^2 dynamo is modified by a weak differential rotation. Even for a weak differential rotation, the behaviour of the magnetic activity is changed drastically from aperiodic regime to nonlinear oscillations and appearance of a chaotic behaviour with increase of the differential rotation. Periods of the magnetic cycles decrease with increase of the differential rotation, and they vary from tens to thousand years. This long-term behaviour of the magnetic cycles may be related to the characteristic time of the evolution of the magnetic helicity density of the small-scale field. The performed analysis is based on the mean-field numerical simulations of the $\alpha^2\Omega$ and α^2 dynamos and a developed nonlinear theory of α^2 dynamo.

Key words: dynamo – MHD – Sun: interior — turbulence – activity

1 INTRODUCTION

The cold dwarf stars of the main sequences of the spectral class M composing 70 - 75% of all star population, have smaller sizes ($0.1R_\odot < R < 0.8R_\odot$) in comparison with the sun, smaller masses ($0.08M_\odot < M < 0.55M_\odot$), smaller luminosity ($L \leqslant 0.05L_\odot$) and effective temperatures of 2500–4000 K, where $R_\odot$, $M_\odot$ and $L_\odot$ are the solar radius, mass and luminosity, respectively (Bochanski et al. 2010; Pecaut & Mamajek 2013; Winters et al. 2019; Kochukhov 2021). About 15 – 20 % of these stars have similar magnetic activity as the sun with cold magnetic spots and sporadic flares of very high releasing energy in the form of radiations in wide range of wavelength including thermal and nonthermal X-ray (Hawley et al. 2014; Newton et al. 2017). As the sun, these stars obey differential rotation and have similar atmospheric structure, consisting of photosphere, hot chromosphere and corona (Wright et al. 2018; Gershberg et al. 2020).

According to various observations (Saar & Linsky 1985; Saar 1996; Donati et al. 2003, 2008; Reiners & Basri 2007), slow rotating stars ($\Omega < \Omega_\odot$) have values and structures of the large-scale magnetic field similar to solar magnetic field, where $\Omega_\odot$ is the solar angular velocity. On the other hand, fast rotating stars ($\Omega > 10\Omega_\odot$) have strong poloidal magnetic fields at the pole, and sometimes they have strong toroidal magnetic fields at the pole (Strassmeier 2009; Morin et al. 2010). The periods of the stellar cycles can be in several times larger than the periods of the solar cycles (Bondar' et al. 2019). Magnetic fields of fast rotating stars can be more than several thousands Gauss (Kochukhov et al. 2020; Kochukhov 2021).

Various MHD simulations of convection and dynamos in low-mass convective stars have been performed in a number of studies (Dobler et al. 2006; Browning 2008; Yadav et al. 2016; Brown et al. 2020; Käpylä 2021; Bice & Toomre 2022). They use fully compressible MHD system with weak density stratification or anelastic simulations with strong density stratification in a box or spherical shell. Main results of these simulations are summarised in review by Käpylä et al. (2023). In particular, when the magnetic field is weak or absent, both "solar" and "anti-solar" differential rotation can be formed. When the dynamo generated large-scale magnetic field is strong, it reduces the differential rotation sometimes resulting to the solid-body rotation.

The dynamo generated large-scale magnetic field is mainly axisymmetric, and it has the dipole or quadrupole structure depending on rotation, shear, and density stratification. In particular, when rotation is strong and shear is weak, the magnetic field has dipolar structure (Gastine et al. 2012; Schrinner et al. 2012; Yadav et al. 2015). There are many simulations with highly-stratified, vigorous convection that also show dipole magnetic structure (Yadav et al. 2015). In the presence of large-scale shear, propagating dynamo waves are observed in simulations (Yadav et al. 2016; Käpylä 2021; Bice & Toomre 2022). Some simulations also produce non-axisymmetric magnetic field (Käpylä 2021; Bice & Toomre 2022).

Various mean-field dynamo models have been suggested to explain generation of large-scale magnetic fields in M dwarfs (Chabrier & Küker 2006; Kitchatinov et al. 2014; Shulyak et al. 2015; Pipin 2017; Pipin & Yokoi 2018). In particular, mean-field simulations of the α^2 dynamo have been performed by Chabrier & Küker (2006). They consider a fully convective rotating star and focus on the kinematic dynamo problem. The large-scale magnetic field is excited when the Coriolis number $\mathrm{Co} = 2\Omega_* \tau \geqslant 1$, and the dynamo generates a non-axisymmetric steady magnetic field that is symmetric with respect to the equatorial plane (Chabrier & Küker 2006).

Kitchatinov et al. (2014) suggest that M-dwarfs have two types of magnetic activity: (i) magnetic cycles with strong (kilogauss) almost axisymmetric poloidal magnetic fields; and (ii) considerably weaker non-axisymmetric fields with a substantial toroidal component observed at times of magnetic field inversion. To show this, they use a kinematic model of an $\alpha^2\Omega$ dynamo with the differential rotation determined using the numerical mean-field model by Kitchatinov & Olemskoy (2011). Applying this model, they study a magnetic field evolution and find a transition from steady to oscillatory dynamos with increasing turbulent magnetic Prandtl number. Using this approach, Shulyak et al. (2015) suggest four magnetic configurations that appear relevant to dwarfs from the viewpoint of the dynamo theory, and discuss observational tests to identify the configurations observationally.

Pipin (2017) has performed mean-field numerical simulations with the nonlinear axisymmetric and non-axisymmetric $\alpha\Omega$ dynamos of the fully convective star with the mass $M = 0.3 M_\odot$ rotating with a period of 10 days. The differential rotation is determined using the numerical mean-field model similar to Kitchatinov & Olemskoy (2011). This dynamo model also includes the meridional circulation, while the magnetic feedback on the non-axisymmetric flows is neglected. The dynamical quenching of the α effect is described by equation for the total magnetic helicity density rather than that for the evolution of magnetic helicity density of the small-scale field. The latter is a weak point of this nonlinear dynamo model, because magnetic α effect is determined by the evolution of current helicity of the small-scale field, which is caused by the evolution of magnetic helicity density of the small-scale field. These mean-field numerical simulations yield different dynamo solutions depending on parameters, including variations of the turbulent magnetic Prandtl number, as a key parameter. Increase of this parameter increases the period of the magnetic cycles.

In the present theoretical study and mean-field numerical simulations, we show that for the main sequences low-mass fast rotating stars, the generated large-scale magnetic field is due to the mean-field $\alpha^2\Omega$ dynamo, in which the α^2 dynamo is modified by a weak differential rotation. We find that periods of the magnetic activity cycles decrease with increase of the differential rotation, and they vary from tens to thousand years. The dynamical quenching of the α effect due to the evolution of the magnetic helicity density of the small-scale field, determines a long-term behaviour of the magnetic cycles. This paper is organized as follows. In Sec. 2 we consider the radial profiles of turbulent parameters in a the stellar convective zones, and discuss the theoretical rotating profiles of the kinetic α effect obtained using theory of the convecting rotating MHD turbulence (Kleeorin & Rogachevskii 2003). In Sec. 3 we study mean-field $\alpha^2\,\Omega$ dynamo, where we start with the kinematic $\alpha^2\,\Omega$ dynamo (Sec. 3.1), and continue with mean-field numerical simulations of the $\alpha^2\Omega$ dynamo (Sec. 3.2) as well as the α^2 dynamo (Sec. 3.3). In Sec. 4 we develop nonlinear theory of axisymmetric α^2 dynamo. Finally, in Sec. 5 we outline conclusions.

2 RADIAL PROFILES OF TURBULENT PARAMETERS IN A THE STELLAR CONVECTIVE ZONES

In this Section, we discuss radial profiles of various turbulent parameters in a the stellar convective zones. As a turbulent model of stellar convective zones, we use "Modules for Experiments in Stellar Astrophysics (MESA)" (Paxton et al. 2011). MESA (http://mesa.sourceforge.net/) is one-dimensional stellar evolution module, which combines many of the numerical and physics modules for simulations of a wide range of stellar evolution scenarios ranging from very low mass to massive stars.

MESA includes a module which implements the standard mixing length theory (MLT) of convection (Cox & Giuli 1968), as well as the modified MLT (Henyey et al. 1965). Whereas the standard MLT assumes high optical depths and no radiative losses, the modified MLT allows the convective efficiency to vary with the opaqueness of the convective element, which is an important effect for convective zones near the outer layers of stars (Henyey et al. 1965).

Using MESA, we plot the radial profiles of the convective turbulent velocity u_c (Fig. 1), the turbulent magnetic diffusivity $\eta_{_T}$ (Fig. 2) and the Coriolis parameter $\Omega_\odot \tau(r)$ (Fig. 3) based on the stellar angular velocity $\Omega_\odot$ and the turbulent turn-over time $\tau(r) = 3\eta_{_T}/u_c^2$ for stars of late spectral classes: M6, M4, M2, K7, K4, K2, and G2. Here H_* is the thickness of the convective zone, h is the hight from the bottom of the convective zone, the velocity is measured in cm/s and R_* is the star radius. Depending on the spectral class and the depth of the convective zone, the convective turbulent velocity u_c changes from 10^2 cm/s to 10^5 cm/s. Strong changes in u_c occur in the upper part of the convective zone (see Fig. 1).

On the other hand, the turbulent magnetic diffusivity $\eta_{_T}$ varies inside the convective zone only in several times for stars of the spectral classes from M2 to G2, while it changes by two orders of magnitude for stars of the spectral

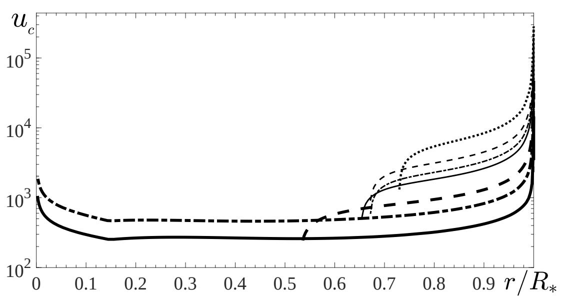

Figure 1. The radial profiles of the convective turbulent velocity u_c for the main sequences stars of the spectral classes: M6 (thick solid); M4 (thick dashed-dotted); M2 (thick dashed); K7 (thin solid); K4 (thin dashed-dotted); K2 (thin dashed); G2 (thin dotted). The velocity is measured in cm/s. Here R_* is the star radius.

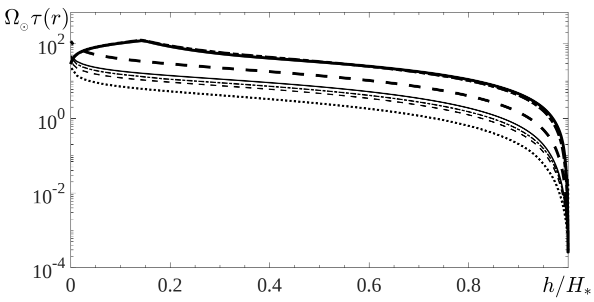

Figure 3. The radial profiles of the Coriolis parameter $\Omega_\odot\tau(h)$ based on the solar angular velocity $\Omega_\odot$ and the turbulent turnover time $\tau(r) = 3\eta_{_T}/u_c^2$ for the main sequences stars of the spectral classes: M6 (thick solid); M4 (thick dashed-dotted); M2 (thick dashed); K7 (thin solid); K4 (thin dashed-dotted); K2 (thin dashed); G2 (thin dotted). The turbulent magnetic diffusivity is measured in cm^2/s.

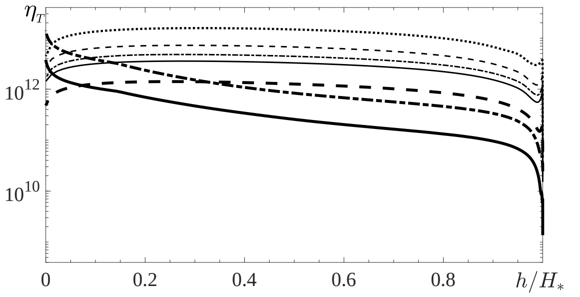

Figure 2. The radial profiles of the turbulent magnetic diffusivity $\eta_{_T}$ for the main sequences stars of the spectral classes: M6 (thick solid); M4 (thick dashed-dotted); M2 (thick dashed); K7 (thin solid); K4 (thin dashed-dotted); K2 (thin dashed); G2 (thin dotted). The turbulent magnetic diffusivity is measured in cm^2/s. Here H_* is the thickness of the convective zone, and h is the hight from the bottom of the convective zone.

classes from M4 and M6 (see Fig. 2). The Coriolis parameter $\Omega_\odot\tau(r)$ based on the solar angular velocity $\Omega_\odot$ and the turbulent turn-over time $\tau(r) = 3\eta_{_T}/u_c^2$ strongly decreases from 10^2 near the base of the convective zone to $10^{-2} - 10^{-4}$ near the star surface depending on the spectral class (see Fig. 3). Note that models of the solar convective zone are given by Baker & Temesvary (1966); Spruit (1974).

Models of the stellar convective zones based on the standard mixing length theory do not take into account the effect of the Coriolis force on the convective turbulence. One of the key effects of rotation in density-stratified convection is

- production of the kinetic helicity and the kinetic α effect,
- formation of the differential rotation and
- strong anisotropization of turbulence.

Using the results obtained applying the theory of the convecting rotating MHD turbulence (Kleeorin & Rogachevskii 2003; Brandenburg et al. 2013), we plot in Figs. 4–7 the isotropic part of the kinetic $\boldsymbol{\alpha}$ tensor that characterises the kinetic $\boldsymbol{\alpha}$ effect,

$$\alpha \quad = \quad \frac{1}{6}\left(\frac{\ell_0^2\Omega}{H_\rho}\right)\sin\phi\,\left[\Psi_1(\omega) + \Psi_2(\omega)\sin^2\phi\right], \tag{1}$$

where ϕ is the latitude, Ω is the angular velocity, H_ρ is the density stratification hight, ℓ_0 is the integral scale of turbulent convection, the parameter $\omega = 4\Omega\tau(r)$, and the functions $\Psi_1(\omega)$ and $\Psi_2(\omega)$ are given in Appendix A.

For instance, for a slow rotation ($\omega \ll 1$), the kinetic α effect is given by

$$\alpha = \frac{4}{5}\left(\frac{\ell_0^2\Omega}{H_\rho}\right)\left(2 - \frac{\sigma}{3} - \frac{5\lambda}{6}\right)\sin\phi\,, \tag{2}$$

and for fast rotation ($\omega \gg 1$) it is given by

$$\alpha \quad = \quad -\frac{\pi}{32}\left(\frac{\ell_0 u_c}{H_\rho}\right)\left(2\lambda + \frac{\sigma}{3} - 3 + (\sigma - 1)\sin^2\phi\right)\sin\phi, \tag{3}$$

where $u_c = \ell_0/\tau$ is the characteristic turbulent velocity. Here the parameter $\lambda = 2\varepsilon/(\varepsilon + 2)$ is related to the degree of anisotropy ε of turbulent velocity field:

$$\varepsilon = \frac{2}{3}\left(\frac{\langle\mathbf{u}_\perp^2\rangle}{\langle\mathbf{u}_z^2\rangle} - 2\right), \tag{4}$$

$\mathbf{u}_\perp$ is the horizontal turbulent velocity, $\mathbf{u}_z$ is the vertical turbulent velocity (in the direction of gravity). The parameter σ determines the degree of thermal anisotropy. For $\sigma < 1$, the thermal plumes in a convective turbulence have the form of column or thermal jets, while for $\sigma > 1$, the ‘‘pancake” thermal plumes exist in the background turbulent convection.

For example, in Fig. 4 we show the radial profiles of the kinetic α effect at the pole (at the latitude $\varphi = \pi/2$) for isotropic turbulent convection for $\sigma = 1$ and $\varepsilon = 0$, while in Fig. 5 we plot the kinetic α effect at the latitude $\varphi = \pi/6$ for anisotropic turbulent convection for $\sigma = 2$ and $\varepsilon = 1.2$. Various curves in Figs. 4 and 5 correspond to stars of the spectral classes from M6 to G2. We use here the radial profile of the Coriolis parameter $\Omega_\odot\tau(r)$ to determine the radial profile of the kinetic $\boldsymbol{\alpha}$ effect which is the function of the Coriolis parameter. It follows from Figs. 4 and 5 that the maximum value α_* of the kinetic α effect depends on the spectral class at a given rotation rate. For instance, the stars of the spectral class G2 have largest α_*, while the stars of the spectral class M6 have smallest α_*. The anisotropy of the convective turbulence decreases the values of α_* and

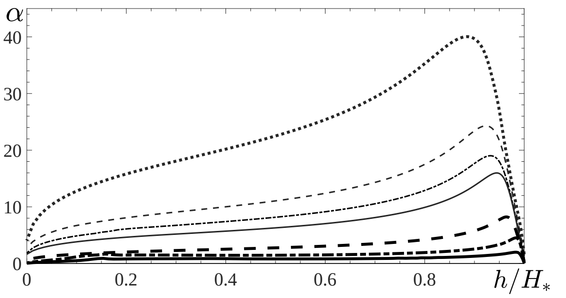

Figure 4. The radial profiles of the kinetic α effect at the pole (at the latitude $\varphi = \pi/2$) for isotropic turbulent convection for $\sigma = 1$ and $\varepsilon = 0$ for the main sequences stars of the spectral classes: M6 (thick solid); M4 (thick dashed-dotted); M2 (thick dashed); K7 (thin solid); K4 (thin dashed-dotted); K2 (thin dashed); G2 (thick dotted). The kinetic α is measured in m/s.

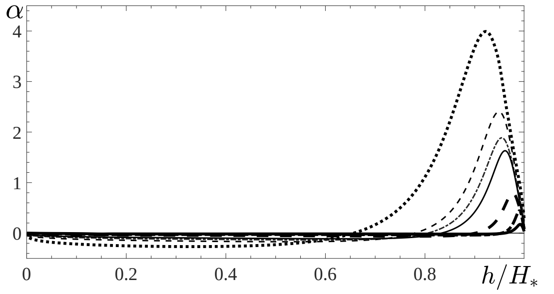

Figure 5. The radial profiles of the kinetic α effect at the latitude $\varphi = \pi/6$ for anisotropic turbulent convection for $\sigma = 2$ and $\varepsilon = 1.2$ for the main sequences stars of the spectral classes: M6 (thick solid); M4 (thick dashed-dotted); M2 (thick dashed); K7 (thin solid); K4 (thin dashed-dotted); K2 (thin dashed); G2 (thick dotted). The kinetic α is measured in m/s.

causes a localization of the maximum value of the kinetic α effect at the vicinity of the star surface and the equator.

The maximum value of the kinetic α effect can be estimated as (Kleeorin et al. 1995)

$$\alpha_* = C_* (\Omega_* \, \eta_{_T})^{1/2}, \tag{5}$$

where the coefficient C_* is given in Table 1 for different spectral classes and different rotation rates. It follows from Table 1 that the coefficient C_α is weakly dependent on the rotation rates. To derive Eq. (5), we use a spatial distribution of the kinetic α effect. In particular, the kinetic α effect is $\alpha \simeq \ell(r)\Omega_*$ for $\ell(r)\Omega_*/u_c(r) \ll 1$, and $\alpha \simeq u_c(r)$ for $\ell(r)\Omega_*/u_c(r) \gg 1$ (Zeldovich et al. 1983). The kinetic α effect has a maximum at the depth $r = r_m$ determined by the condition $\ell_m(r_m) = u_c(r_m)/\Omega_*$. The turbulent magnetic diffusivity is $\eta_{_T} \simeq \ell_m(r_m) u_c(r_m)$. Therefore, $\ell_m(r_m) \simeq (\eta_{_T}/\Omega_*)^{1/2}$. The maximal value of the kinetic α effect, α_*, is given by $\alpha_* \simeq u_c(r_m) \simeq \eta_{_T}/\ell_m(r_m) \simeq (\eta_{_T}\Omega_*)^{1/2}$.

Table 1. The coefficient C_* for different spectral classes and different rotation rates.

spectral class	$\Omega_\odot$	$10\Omega_\odot$	$20\Omega_\odot$
G2	0.970	0.933	0.982
K2	0.877	0.874	0.883
K4	0.824	0.858	0.854
K7	0.855	0.815	0.793
M2	0.643	0.687	0.680

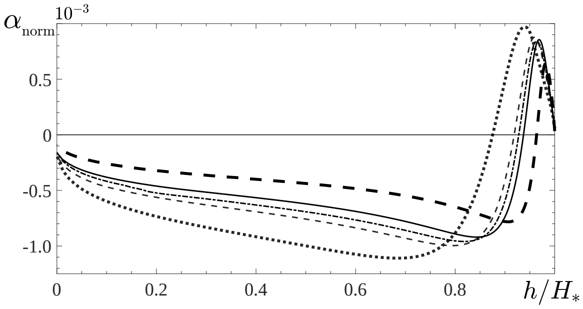

Figure 6. The radial profiles of the normalized kinetic α effect, $\alpha_{\rm norm} = \alpha/(\Omega_\odot \, \eta_{_T})^{1/2}$, at the pole ($\varphi = \pi/2$) for $\sigma = 2$ and $\varepsilon = 1.2$, for the main sequences stars with the solar rotation rate of the spectral classes: M6 (thick solid); M4 (thick dashed-dotted); M2 (thick dashed); K7 (thin solid); K4 (thin dashed-dotted); K2 (thin dashed); G2 (thick dotted). Here H_* is the hight of the convective zone, and h is the hight from the bottom of the convective zone.

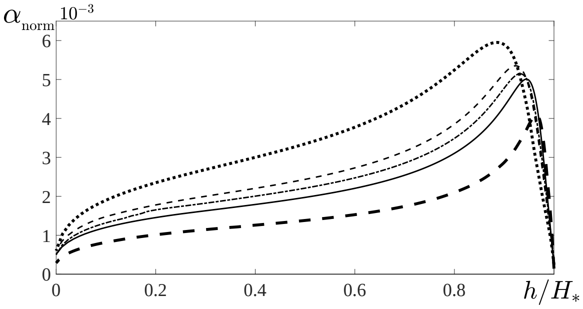

Figure 7. The radial profiles of the normalized kinetic α effect, $\alpha_{\rm norm} = \alpha/(10\Omega_\odot \, \eta_{_T})^{1/2}$, at the pole ($\varphi = \pi/2$) for $\sigma = 1$ and $\varepsilon = 0$, for the main sequences stars of the spectral classes: M6 (thick solid); M4 (thick dashed-dotted); M2 (thick dashed); K7 (thin solid); K4 (thin dashed-dotted); K2 (thin dashed); G2 (thick dotted). Here H_* is the hight of the convective zone, and h is the hight from the bottom of the convective zone.

In Figs. 6–7 we show the radial profiles $\alpha_{\rm norm} = \alpha/(\Omega_\odot \, \eta_{_T})^{1/2}$ of the kinetic α effect normalized by $(\Omega_\odot \, \eta_{_T})^{1/2}$. This normalization and anisotropy of the convective turbulence cause the curves of the different spectral classes $\alpha_{\rm norm}$ almost collapse to each other. This indicates that the estimate (5) is enough good. In the present study we will use this estimate to determine the dynamo number (see below).

3 MEAN-FIELD $\alpha^2\Omega$ DYNAMO

Mean-field theories of solar, stellar and galactic dynamos have been developing during last 55 years (see, e.g., books by Moffatt 1978; Parker 1979; Krause & Rädler 1980; Zeldovich et al. 1983; Ruzmaikin et al. 1988; Rüdiger et al. 2013; Moffatt & Dormy 2019; Rogachevskii 2021; Shukurov & Subramanian 2021). In the present study, we show that magnetic field generation in fast rotating stars of the spectral classes: from M6 to G0 can be described by the axisymmetric mean-field $\alpha^2\,\Omega$ dynamo. The axisymmetric large-scale magnetic field can be written as $\overline{\boldsymbol{B}} = \overline{B}_\varphi \boldsymbol{e}_\varphi + \boldsymbol{\nabla}\times(\overline{\mathsf{A}}\boldsymbol{e}_\varphi)$, where (r, θ, φ) are the spherical coordinates. We consider the mean-field dynamo in a thin convective shell, taking into account strong variation of the plasma density in the radial direction by averaging the equations for the mean toroidal field $\overline{B}_\varphi$ and the magnetic potential $\overline{\mathsf{A}}$ of the mean poloidal field over the depth of the convective shell. We neglect the curvature of the convective shell and replace it by a flat slab. Thus, the mean-field $\alpha^2\,\Omega$ dynamo equations are given by:

$$\frac{\partial \overline{B}_\varphi}{\partial t} = \left[R_\alpha\, R_\omega\, \sin\theta \frac{\partial}{\partial\theta} - R_\alpha^2 \left(\frac{\partial^2}{\partial\theta^2} - \mu^2\right)\right]\overline{A} + \left(\frac{\partial^2}{\partial\theta^2} - \mu^2\right)\overline{B}_\varphi, \tag{6}$$

$$\frac{\partial \overline{A}}{\partial t} = \alpha\overline{B}_\varphi + \left(\frac{\partial^2}{\partial\theta^2} - \mu^2\right)\overline{A}. \tag{7}$$

To take into account strong variation of the plasma density in the radial direction, we average the dynamo equations over the depth of the convective zone and use the no-z model. In particular, the terms describing turbulent diffusion of the mean magnetic field in the radial direction in equations (6) and (7) in the framework of the no-z model are given as $-\mu^2\overline{B}_\varphi$ and $-\mu^2\overline{A}$ (Kleeorin et al. 2003a, 2016; Safiullin et al. 2018). The differential rotation is characterised by parameter $G = \partial\Omega/\partial r$, and the parameter μ is determined by the following equation: $\int_{r_{\rm c}}^1 (\partial^2\overline{B}_\varphi/\partial r^2)\, dr = -(\mu^2/3)\overline{B}_\varphi$.

Equations (6)–(7) are written in dimensionless variables: the coordinate r is measured in the units of the star radius R_*, the time t is measured in the units of turbulent magnetic diffusion time $R_*^2/\eta_{_T}$; the toroidal component, $\overline{B}_\varphi(t, r, \theta)$, of the mean magnetic field is measured in the units of B_*, where $B_* \equiv \xi\, \overline{B}_{\rm eq}$, $\xi = \ell_0/\sqrt{2}R_*$ and $\overline{B}_{\rm eq} = u_0\,\sqrt{4\pi\overline{\rho}_*}$. The magnetic potential, $\overline{A}(t, r, \theta)$, of the poloidal field is measured in the units of $R_\alpha R_* B_*$, where $R_\alpha = \alpha_* R_*/\eta_{_T}$, the fluid density $\overline{\rho}(r, \theta)$ is measured in the units $\overline{\rho}_*$, the differential rotation $\delta\Omega$ is measured in units of the maximal value of the angular velocity Ω, the α effect is measured in units of the maximum value of the kinetic α effect, α_*; the integral scale of the turbulent motions ℓ_0 and the characteristic turbulent velocity u_0 at the scale ℓ_0 are measured in units of their maximum values in the convective region. The magnetic Reynolds number ${\rm Rm} = \ell_0\, u_0/\eta$ is defined using the maximal values of the integral scale ℓ_0 and the characteristic turbulent velocity u_0, and the turbulent magnetic diffusion coefficient is $\eta_{_T} = \ell_0\, u_0/3$. The dynamo number is defined as $D = R_\alpha R_\omega$, where $R_\omega = (\delta\Omega)\, R_*^2/\eta_{_T}$.

Equations (6) and (7) describe the dynamo waves propagating from the central latitudes towards the equator when the dynamo number is negative. The radius r varies from $r_{\rm c}$ to 1 inside the convective shell, so that, e.g., for stars of the spectral class G2 (the solar-like stars), the value $\mu = 3$ corresponds to a convective zone with a thickness of about 1/3 of the radius.

3.1 Kinematic $\alpha^2\,\Omega$ dynamo

First, we consider a kinematic dynamo problem, assuming for simplicity that the kinetic α effect is a constant. We seek a solution for Eqs. (6)–(7) as a real part of the following functions:

$$\overline{A} = A_0 \exp(\tilde\gamma t - {\rm i}\, k\, \theta), \tag{8}$$

$$\overline{B}_\varphi = B_0 \exp(\tilde\gamma t - {\rm i}\, k\, \theta), \tag{9}$$

where $\tilde\gamma = \gamma + {\rm i}\,\omega$. Equations (6)–(9) yield the growth rate of the dynamo instability and the frequency of the dynamo waves as

$$\gamma = \frac{R_\alpha R_\alpha^{\rm cr}}{\sqrt{2}} \left[\left[1 + \left(\frac{\zeta R_\omega}{R_\alpha R_\alpha^{\rm cr}}\right)^2\right]^{1/2} + 1\right]^{1/2} - \left(R_\alpha^{\rm cr}\right)^2, \tag{10}$$

$$\omega = -{\rm sgn}(R_\omega)\, \frac{R_\alpha R_\alpha^{\rm cr}}{\sqrt{2}} \left[\left[1 + \left(\frac{\zeta R_\omega}{R_\alpha R_\alpha^{\rm cr}}\right)^2\right]^{1/2} - 1\right]^{1/2}, \tag{11}$$

where $\zeta^2 = 1 - (\mu/R_\alpha^{\rm cr})^2$. Here we took into account that $(x + {\rm i}y)^{1/2} = \pm(X + {\rm i}Y)$, where $X = 2^{-1/2}\,[(x^2 + y^2)^{1/2} + x]^{1/2}$ and $Y = {\rm sgn}(y)\, 2^{-1/2}\,[(x^2 + y^2)^{1/2} - x]^{1/2}$. Here the threshold $R_\alpha^{\rm cr}$ for the mean-field dynamo instability, defined by the conditions $\gamma = 0$ and $R_\omega = 0$, is given by $R_\alpha^{\rm cr} = (k^2 + \mu^2)^{1/2}$.

Equations (6)–(9) allow one to determine the squared amplitude ratio $|A_0/B_0|^2$ as

$$\left|\frac{A_0}{B_0}\right|^2 = \left(R_\alpha R_\alpha^{\rm cr}\right)^{-2} \left(1 + \zeta^2 R_\omega^2\right)^{-1}, \tag{12}$$

and the phase shift between the toroidal field $\overline{B}_\varphi$ and the poloidal field $\overline{B}_\theta$ as

$$\sin(2\delta) = -\zeta R_\omega\, \left[\left(R_\alpha R_\alpha^{\rm cr}\right)^2 + \zeta^2 R_\omega^2\right]^{-1/2}. \tag{13}$$

Equation (12) yields the energy ratio of poloidal $\overline{B}_{\rm pol} = R_\alpha R_\alpha^{\rm cr}\, \overline{A}$ and toroidal $\overline{B}_\varphi$ mean magnetic field components as

$$\frac{\overline{B}_{\rm pol}^2}{\overline{B}_\varphi^2} = \left(1 + \zeta^2 R_\omega^2\right)^{-1}. \tag{14}$$

Asymptotic formulas for the growth rate of the dynamo instability and the frequency of the dynamo waves for a weak differential rotation, $\zeta R_\omega \ll R_\alpha R_\alpha^{\rm cr}$, are given by

$$\gamma = R_\alpha R_\alpha^{\rm cr} \left[1 + \frac{1}{8}\left(\frac{\zeta R_\omega}{R_\alpha R_\alpha^{\rm cr}}\right)^2\right] - \left(R_\alpha^{\rm cr}\right)^2, \tag{15}$$

$$\omega = -\frac{\zeta R_\omega}{\sqrt{2}}. \tag{16}$$

In this case, the mean-field α^2 dynamo is slightly modified by a weak differential rotation, and the phase shift between the fields $\overline{B}_\varphi$ and $\overline{B}_\theta$ vanishes, while $\overline{B}_{\rm pol}/\overline{B}_\varphi \sim 1$ [see Eqs. (13)–(14)]. The period of the dynamo wave is $T_{\rm dyn} = (2\pi/\omega)\, (R_*^2/\eta_{_T})$, where ω is the non-dimensional frequency of the dynamo wave given by Eq. (16). In the present study, we show that this case corresponds to fast rotating stars of the spectral class from M6 to G0. Since in this case $\overline{B}_{\rm pol} \sim \overline{B}_\varphi$, the star spots can be formed for any latitude.

In the opposite case, for a strong differential rotation, $\zeta R_\omega \gg R_\alpha R_\alpha^{\rm cr}$, the growth rate of the dynamo instability and the frequency of the dynamo waves are given by

$$\gamma = \left[{1 \over 2} \, \zeta \, R_\alpha^{\rm cr} \, R_\alpha |R_\omega|\right]^{1/2} - (R_\alpha^{\rm cr})^2 \,, \tag{17}$$

$$\omega = -{\rm sgn}(R_\omega) \, \left[{1 \over 2} \, \zeta \, R_\alpha^{\rm cr} \, R_\alpha |R_\omega|\right]^{1/2} . \tag{18}$$

In this case the mean-field $\alpha\Omega$ dynamo is slightly modified by a weak α^2 effect, and the phase shift between the fields $\overline{B}_\varphi$ and $\overline{B}_\theta$ tends to $-\pi/4$, while $\overline{B}_{\rm pol}/\overline{B}_\varphi \ll 1$ [see Eqs. (13)–(14)]. This case corresponds to the solar dynamo. The necessary condition for the dynamo ($\gamma > 0$) is

(a) when $R_\alpha / R_\alpha^{\rm cr} < \sqrt{2}$, the mean-field $\alpha^2 \, \Omega$ dynamo is excited when

$$D > {2 \over \zeta} \, (R_\alpha^{\rm cr})^3 \,; \tag{19}$$

(b) when $R_\alpha / R_\alpha^{\rm cr} > \sqrt{2}$, the mean-field $\alpha^2 \, \Omega$ dynamo is excited for any differential rotation, R_ω.

3.2 Mean-field numerical simulations of the $\alpha^2\Omega$ dynamo

The total α effect is the sum of the kinetic and magnetic α effects,

$$\alpha = \chi_{_{\rm K}} \Phi_{_{\rm K}}(\overline{B}) + \sigma \chi_{_{\rm M}} \Phi_{_{\rm M}}(\overline{B}), \tag{20}$$

where $\chi_{_{\rm K}} = -(\tau_0/3) \, \langle \boldsymbol{u} \cdot (\boldsymbol{\nabla} \times \boldsymbol{u}) \rangle$ is proportional to the kinetic helicity $\langle \boldsymbol{u} \cdot (\boldsymbol{\nabla} \times \boldsymbol{u}) \rangle$ and $\chi_{_{\rm M}} = (\tau_0 / 12 \pi \overline{\rho}) \, \langle \boldsymbol{b} \cdot (\boldsymbol{\nabla} \times \boldsymbol{b}) \rangle$ is proportional to the current helicity $\langle \boldsymbol{b} \cdot (\boldsymbol{\nabla} \times \boldsymbol{b}) \rangle$ (Frisch et al. 1975; Pouquet et al. 1976). Here τ_0 is the correlation time of the turbulent velocity field, $\boldsymbol{u}$ and $\boldsymbol{b}$ are velocity and magnetic fluctuations, and $\sigma = \int_{r_{\rm c}}^1 (\overline{\rho}(r)/\overline{\rho}_*)^{-1} \, dr$ (Kleeorin et al. 2016; Safiullin et al. 2018).

The quenching functions $\Phi_{_{\rm K}}(\overline{B})$ and $\Phi_{_{\rm M}}(\overline{B})$ in equation for the total α effect are given by (Rogachevskii & Kleeorin 2000, 2001, 2004),

$$\Phi_{_{\rm K}}(\overline{B}) = {1 \over 7} \left[4 \Phi_{_{\rm M}}(\overline{B}) + 3 \Phi_{_{\rm B}}(\overline{B})\right] , \tag{21}$$

and (Field et al. 1999)

$$\Phi_{_{\rm M}}(\overline{B}) = {3 \over 8 \beta^2} \left[1 - {\arctan (\sqrt{8} \beta) \over \sqrt{8} \beta}\right] , \tag{22}$$

where $\beta = \overline{B}/\overline{B}_{\rm eq}$

$$\Phi_{_{\rm B}}(\overline{B}) = 1 - 16 \beta^2 + 128 \beta^4 \ln \left[1 + (8\beta^2)^{-1}\right] , \tag{23}$$

and $\chi_{_{\rm K}}$ and $\chi_{_{\rm M}}$ are measured in units of maximal value of the α-effect, α_*. The function $\Phi_{_{\rm K}}$ describes the algebraic quenching of the kinetic α effect that is caused by the feedback effects of the mean magnetic field on plasma motions. The densities of the kinetic and current helicities, and quenching functions are associated with a middle part of the convective zone. The parameter $\sigma > 1$ is a free parameter.

The magnetic α effect, $\alpha_{_{\rm M}}$, is based on two nonlinearities: the algebraic nonlinearity given by the quenching function $\Phi_{_{\rm M}}(\overline{B})$, and the dynamic nonlinearity, characterised by the function $\chi_{_{\rm M}}(\overline{\boldsymbol{B}})$ that is determined by a non-dimensional dynamical equation (Kleeorin & Ruzmaikin 1982; Gruzinov & Diamond 1994; Kleeorin & Rogachevskii 1999; Kleeorin et al. 1995, 2000, 2002, 2003a,b; Blackman & Field 2000; Brandenburg & Subramanian 2005; Zhang et al. 2006, 2012):

$$\begin{aligned} {\partial \chi_{\rm c} \over \partial t} + \left(\tau_\chi^{-1} + \kappa_{_T} \mu^2\right) \chi_{\rm c} &= 2 \left({\partial \overline{\mathsf{A}} \over \partial \theta} {\partial \overline{B}_\varphi \over \partial \theta} + \mu^2 \overline{\mathsf{A}} \, \overline{B}_\varphi \right) \\ &\quad - \alpha \, \overline{B}^2 - {\partial \over \partial \theta} \left(\overline{B}_\varphi {\partial \overline{\mathsf{A}} \over \partial \theta} - \kappa_{_T} \, {\partial \chi^c \over \partial \theta}\right) , \end{aligned} \tag{24}$$

where $\boldsymbol{F}_\chi = - \kappa_{_T} \boldsymbol{\nabla} \chi_{\rm c}$ is the turbulent diffusion flux of the density of the magnetic helicity, $\kappa_{_T}$ is the coefficient of the turbulent diffusion of the magnetic helicity, $\tau_\chi = \ell^2/\eta$ is the relaxation time of magnetic helicity. This equation is derived from the conservation law for magnetic helicity for very small magnetic diffusivity η. The average value of τ_χ^{-1} is given by

$$\tau_\chi^{-1} = H_*^{-1} \int_{r_{\rm c}}^1 \tilde \tau_\chi^{-1}(r) \, dr \sim {H_\ell \, R_*^2 \, \eta \over H_* \, \ell^2 \, \eta_{_T}} , \tag{25}$$

where H_* is the depth of the convective zone, H_ℓ is the characteristic scale of variations ℓ_0, and $\tilde \tau_\chi(r) = (\eta_{_T}/R_*^2) (\ell_0^2/\eta)$ is the non-dimensional relaxation time of the density of the magnetic helicity. The values H_ℓ, η, ℓ_0 in equation (25) are associated with the upper part of the convective zone. The mean magnetic field is given by

$$\overline{B}^2 = \overline{B}_\varphi^2 + R_\alpha^2 \left[\mu^2 \overline{\mathsf{A}}^2 + \left({\partial \overline{\mathsf{A}} \over \partial \theta}\right)^2\right] . \tag{26}$$

We solve numerically Eqs. (6), (7) and (24). For numerical simulations, we use the standard profile of the kinetic α effect: $\alpha(\theta) = \alpha_0 \sin^3 \theta \cos \theta$. The parameters of the numerical simulation are as follows: $G = 1$, $\sigma = 3$, , $\xi = 0.1$, $\kappa_{_T} = 0.1$, $T = 6.3$, $S_1 = 0.051$, $S_2 = 0.95$ for different μ, R_α and R_ω. We use the following initial conditions: $\overline{B}_\phi(t=0, \theta) = S_1 \sin \theta + S_2 \sin(2\theta)$ and $\overline{\mathsf{A}}(t=0, \theta) = 0$ corresponding to a combination of the dipole and quadropole type solutions. These parameters and initial conditions have been used by us for modelling of the solar activity by the axisymmetric mean-field $\alpha \, \Omega$ dynamo (Kleeorin et al. 2016, 2020; Safiullin et al. 2018), where mechanism of the sunspot formation related to negative effective magnetic pressure instability have been taken into account (Kleeorin et al. 1989, 1990, 1996; Kleeorin & Rogachevskii 1994; Rogachevskii & Kleeorin 2007; Brandenburg et al. 2011, 2016; Warnecke et al. 2013).

First we perform numerical simulations of the $\alpha^2\Omega$ mean-field dynamo at $R_\alpha = 10$. This value of the parameter R_α corresponds to the kinetic α effect arising in rotating convective turbulence with the rotating frequency that is in 25 times larger than that for the sun. In Fig. 8 we plot the ratio of the maximum values of the poloidal to toroidal mean magnetic fields $\overline{B}_{\rm pol}/\overline{B}_{\rm tor}$ versus R_ω/R_α. Depending on the ratio R_ω/R_α, there are ranges of the aperiodic behavior, the quasi-periodic oscillations of the mean magnetic field and the chaotic behaviour. This is seen in Fig. 9, where we show the time evolution of the flux of the toroidal mean magnetic field $\Phi = \int |\overline{B}_\varphi| \, d\sigma$ obtained from numerical simulations of the $\alpha^2\Omega$ mean-field dynamo for different values of R_ω/R_α =1.6; 3.2; 4.7 and 6.4. The time is normalized by

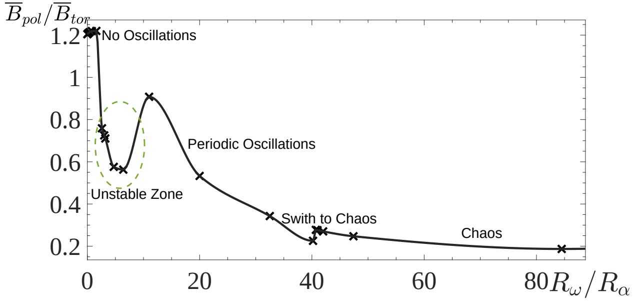

Figure 8. The ratio of the maximum values of the poloidal to toroidal mean magnetic fields $\overline{B}_{\rm pol}/\overline{B}_{\rm tor}$ versus R_ω/R_α obtained from numerical simulations of $\alpha^2\Omega$ mean-field dynamo.

122.2 years, and the flux Φ is normalized by the magnetic field of 300 G.

Note that 122.2 years corresponds to the turbulent diffusion time $R_*^2/\eta_{_T}$ with $R_* = R_\odot$ and $\eta_{_T} = 1.4 \times 10^{12}$ cm^2/s. Here we take into account that the integral scale ℓ_0 of the turbulent convection is smaller by a factor 5 – 7 than the size of the coherent structures (the large-scale circulations). The latter is justified by the results of analytical study (Elperin et al. 2002, 2006) and laboratory experiments (Bukai et al. 2009). This causes the mixing length used in the mixing length theory is about 5 –7 times larger than the integral scale ℓ_0 of the turbulent convection. Correspondingly, the turbulent diffusion coefficients should be 5 –7 times smaller than those from the mixing length theory.

Increase of R_ω/R_α causes decrease the periods T_* of the stellar magnetic cycles. This is seen in Fig. 10, where we show the periods T_* of the stellar magnetic cycles normalized by 122.2 years versus R_ω/R_α, which decreases from about 10^3 years to 10 years depending on the value of the differential rotation. In chaotic regime there can be transition from one attractor with a short period (of several tens years) to that of a larger period (of thousand years), see Fig. 9c. For larger values of R_ω/R_α, the dynamo is similar to the $\alpha\Omega$ mean-field dynamo, while for small values of R_ω/R_α, the dynamo is similar to the α^2 mean-field dynamo.

We will show in the next section that for low-mass main sequences stars rotating much faster than the sun, the generated large-scale magnetic field is caused by the mean-field $\alpha^2\Omega$ dynamo, whereby the α^2 dynamo is slightly modified by a weak differential rotation in comparison with the sun.

3.3 Mean-field numerical simulations of the α^2 dynamo

We also perform numerical simulations of the α^2 mean-field dynamo with $R_\omega = 0$. First, we plot the threshold, $R_\alpha^{\rm cr}$, required for the generation of the large-scale magnetic field versus

- parameter μ (Fig. 11),
- the spectral class (Fig. 12) and
- the stellar effective temperature $T_{\rm eff}$ (Fig. 13)

obtained from numerical simulations. For $\mu \geqslant 3$, the function $R_\alpha^{\rm cr}(\mu)$ is closed to the linear one (see Fig. 11). Indeed, our asymptotic analysis for a constant kinetic α effect shows that $R_\alpha^{\rm cr} = (k^2 + \mu^2)^{1/2}$. This implies that when $k^2 \ll \mu^2$, we obtain that $R_\alpha^{\rm cr} \sim \mu$.

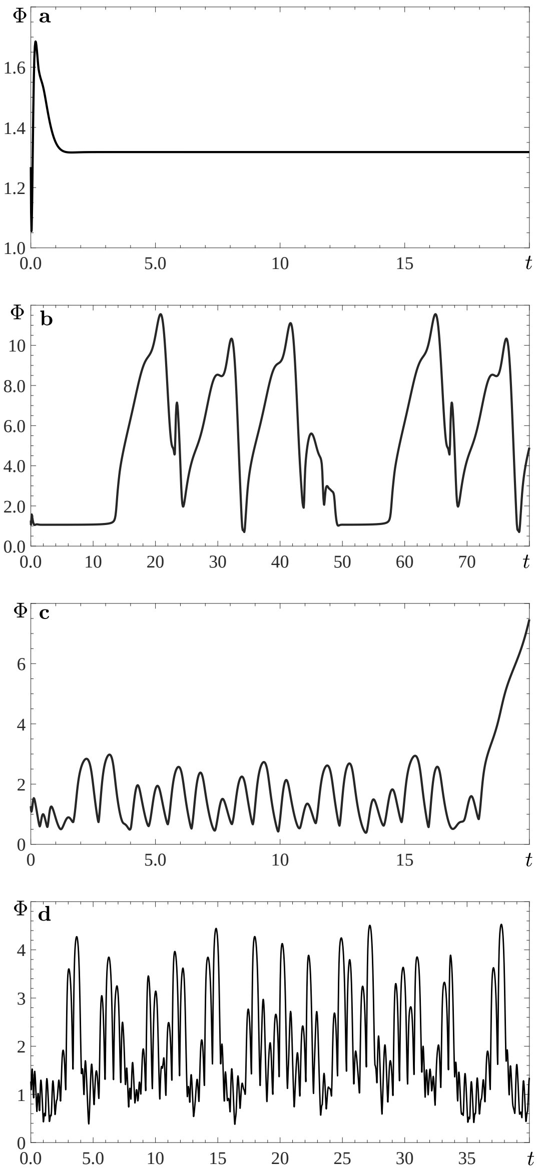

Figure 9. The time evolution of the flux of the toroidal mean magnetic field $\Phi = \int |\overline{B}_\varphi| \, d\sigma$ obtained from numerical simulations of $\alpha^2\Omega$ mean-field dynamo at different values of $R_\omega/R_\alpha =$ 1.6 (**a**); 3.2 (**b**); 4.7 (**c**) and 6.4 (**d**). The time is normalized by 122.2 years, and the flux Φ is normalized by the magnetic field of 300 G.

In Fig. 12, in addition to the threshold $R_\alpha^{\rm cr}$ versus the stellar spectral class, we also plot the parameter $R_\alpha \equiv \alpha_* R_*/\eta_{_T} = (\Omega_\odot/\eta_{_T})^{1/2} \, R_*$ based on the solar rotation rate [see Eq. (5)]. As follows from Fig. 12, the parameter R_α is in several times less than the threshold $R_\alpha^{\rm cr}$ required for the generation of the large-scale magnetic field. This implies that the pure α^2 dynamo with the kinetic α effect $\alpha = (\Omega_\odot \eta_{_T})^{1/2}$ based on the solar rotation rate cannot explain the generation of large-scale magnetic field in the main sequences stars. To describe correctly the magnetic field generation in the main sequences stars in the framework of the α^2 dynamo, one need to increase the stellar rotation rate by one order of

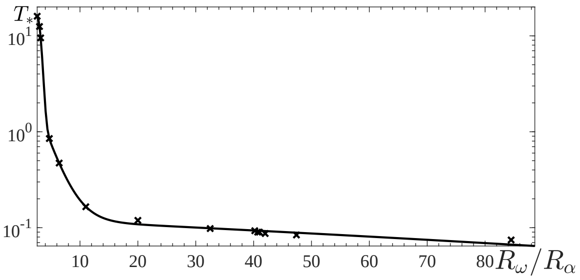

Figure 10. The period T_* of the stellar magnetic cycles normalized by 122.2 years versus R_ω obtained from numerical simulations of the nonlinear $\alpha^2\Omega$ mean-field dynamo at $R_\alpha = 10$.

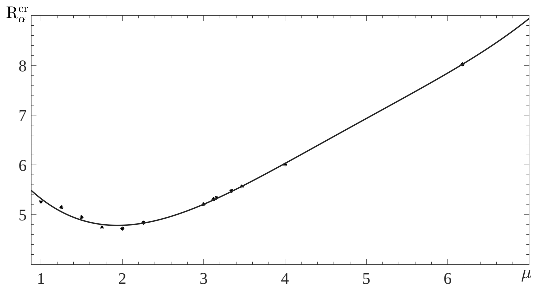

Figure 11. The threshold, $R_\alpha^{\rm cr}$, in generation of the large-scale magnetic field (snowflakes) versus parameter μ obtained from numerical simulations of the nonlinear α^2 mean-field dynamo. Here the solid line corresponds to the fitting curve.

magnitude to obtain the required value of the α effect. That is why we consider stars rotating much faster than the sun.

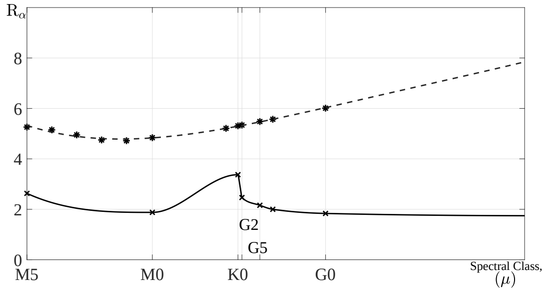

Figure 12. The threshold $R_\alpha^{\rm cr}$ (snowflakes, dashed line) in generation of the large-scale magnetic field and the parameter R_α (crosses, solid line) versus the parameter μ obtained from numerical simulations of the nonlinear α^2 mean-field dynamo. The parameter $R_\alpha = (\Omega_\odot/\eta_T)^{1/2}\, R_*$ is determined for the main sequence stars, where the angular velocity coincides with the mean (averaged over the latitude) solar angular velocity $\Omega_\odot$.

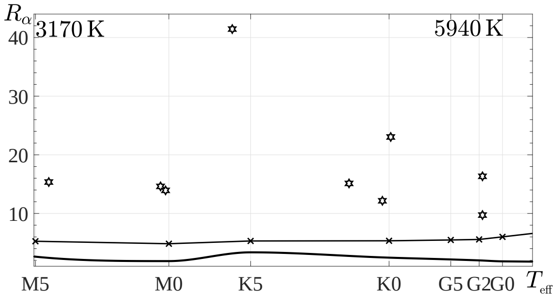

Figure 13. The threshold $R_\alpha^{\rm cr}$ (crosses, thin solid line) in generation of the large-scale magnetic field and the parameter $R_\alpha = (\Omega_\odot/\eta_T)^{1/2}\, R_*$ (solid line) versus the star effective temperature $T_{\rm eff}$ obtained from numerical simulations of the nonlinear α^2 mean-field dynamo. The parameter R_α is calculated for the main sequence stars, where the angular velocity coincides with the mean (averaged over the latitude) solar angular velocity $\Omega_\odot$. The parameter $\tilde R_\alpha$ (stars) is also estimated for real main sequence stars, where the rotating rates (see Gershberg et al. 2021) and turbulent magnetic diffusion coefficients for these stars, and Eq. (5) are used.

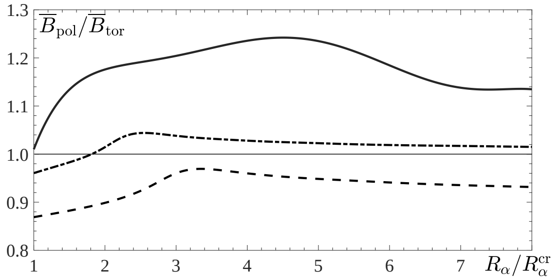

Figure 14. The ratio of the maximum values of the poloidal to toroidal mean magnetic fields $\overline{B}_{\rm pol}/\overline{B}_{\rm tor}$ versus $R_\alpha/R_\alpha^{\rm cr}$ for the main sequence stars of three spectral classes: M5 (solid); M0 (dashed-dotted); K5 (dashed), obtained from numerical simulations of the nonlinear α^2 mean-field dynamo.

In Fig. 13, we show the threshold $R_\alpha^{\rm cr}$ (crosses, thin solid line) in generation of the large-scale magnetic field and the parameter $R_\alpha = (\Omega_\odot/\eta_T)^{1/2}\ R_*$ (thick solid line) versus the star effective temperature $T_{\rm eff}$ obtained from numerical simulations of the nonlinear α^2 mean-field dynamo. This parameter R_α is calculated for the main sequence stars, where the angular velocity coincides with the mean (averaged over the latitude) solar angular velocity $\Omega_\odot$. In addition, we also show the parameter $\tilde R_\alpha$ (shown as stars) that is estimated for real main sequence stars, where we use Eq. (5), the rotating rates (see Gershberg et al. 2021) and turbulent magnetic diffusion coefficients for these stars. Figure 13 demonstrates that the parameter R_α for the observed stars is in several times larger than the threshold $R_\alpha^{\rm cr}$ required for the generation of the large-scale magnetic field by pure α^2 dynamo. This shows that the pure α^2 dynamo can describe the generation of large-scale magnetic field for these stars. However, some observed features (appearance of star spots in the polar regions, long period of cyclic behaviour, etc.) for the main sequence fast rotating stars require presence of small differential rotation.

In Fig. 14 we show the ratio of the maximum poloidal to maximum toroidal mean magnetic field $\overline{B}_{\rm pol}/\overline{B}_{\rm tor}$ versus $R_\alpha/R_\alpha^{\rm cr}$ for the main sequence stars of three spectral classes: M5; M0 and K5, obtained from numerical simulations in nonlinear saturated stage. It seen that in nonlinear saturated stage $\overline{B}_{\rm pol}/\overline{B}_{\rm tor} \sim 1$. This is in agreement with Eq. (14) derived for the kinematic mean-field dynamo.

4 NONLINEAR THEORY OF AXISYMMETRIC α^2 DYNAMO

In this section we discuss a nonlinear theory of axisymmetric α^2 dynamo. We consider the axisymmetric mean-field α^2 dynamo in spherical coordinates (r, θ, φ). The nonlinear mean-field induction equation reads

$$\frac{\partial}{\partial t} \begin{pmatrix} A \\ B \end{pmatrix} = \left(\hat{L} + \hat{N}\right) \begin{pmatrix} A \\ B \end{pmatrix}, \tag{27}$$

where

$$\hat{L} = \begin{pmatrix} \Delta_{\rm s} & \alpha_{\rm k}(r,\theta) \\ -R_\alpha^2 \Delta_{\alpha_{\rm k}} & \Delta_{\rm s} \end{pmatrix}, \tag{28}$$

$$\hat{N} = \begin{pmatrix} 0 & \alpha_{\rm m}(r,\theta) \\ -R_\alpha^2 \Delta_{\alpha_{\rm m}} & 0 \end{pmatrix}, \tag{29}$$

and

$$\begin{aligned} \Delta_{\rm s} \tilde{\Phi} &= \frac{1}{r} \frac{\partial^2}{\partial r^2} (r \tilde{\Phi}) + \frac{1}{r^2} \frac{\partial}{\partial \theta} \left(\frac{1}{\sin\theta} \frac{\partial}{\partial \theta} (\sin\theta \, \tilde{\Phi}) \right) \\ &\equiv \left(\Delta - \frac{1}{r^2 \sin^2\theta} \right) \tilde{\Phi}, \end{aligned}$$

and

$$\begin{aligned} \Delta_{\alpha_{\rm k,m}} \tilde{\Phi} &= \frac{1}{r} \frac{\partial}{\partial r} \left(\alpha_{\rm k,m} \frac{\partial}{\partial r} (r \tilde{\Phi}) \right) \\ &+ \frac{1}{r^2} \frac{\partial}{\partial \theta} \left(\frac{\alpha_{\rm k,m}}{\sin\theta} \frac{\partial}{\partial \theta} (\sin\theta \, \tilde{\Phi}) \right). \end{aligned}$$

Equations (27)–(29) are written in dimensionless variables (see Section 3). The operator $\hat{L}$ determines the kinematic dynamo. General properties of this operator are briefly presented in Appendix B. Here $\alpha_{\rm k}(r,\theta) = -\alpha_{\rm k}(r, \pi - \theta)$.

We neglect algebraic quenching of the kinetic and magnetic α effect, but take into account the dynamical nonlinearity related to the conservation law of the total magnetic helicity for very large magnetic Reynolds numbers. The magnetic α effect is determined by the evolutionary equation

$$\begin{aligned} \frac{\partial \alpha_{\rm m}}{\partial t} + \frac{\alpha_{\rm m}}{T_\alpha} &= \boldsymbol{\nabla} \cdot (\kappa_{_T} \boldsymbol{\nabla} \alpha_{\rm m}) - \frac{2}{\rho} \Big[(\alpha_{\rm k} + \alpha_{\rm m}) \, R_\alpha^2 \, \overline{\boldsymbol{B}}_p^{\,2} \\ &- \hat{M}(B, A) + B \, \frac{\partial A}{\partial t} \Big], \end{aligned} \tag{30}$$

where $\overline{\boldsymbol{B}}_p = {\rm rot}[A(t, r, \theta) \boldsymbol{e}_\varphi]$ is the poloidal component of the mean magnetic field, and

$$\hat{M}(B, A) = {\rm rot}\,(B \, \boldsymbol{e}_\varphi) \cdot {\rm rot}\,(A \, \boldsymbol{e}_\varphi) \, .$$

We seek a solution of the nonlinear equations (27) and (30) in the following form:

$$\begin{pmatrix} A \\ B \end{pmatrix} = \sum_{n=1}^{\infty} F^n(t) \mathbf{e}_n(r, \theta), \quad \mathbf{e}_n = \begin{pmatrix} a_n \\ b_n \end{pmatrix}, \tag{31}$$

where $\boldsymbol{e}_n$ are the eigenvectors of the operator $\hat{L}$ for $R_\alpha = R_{\alpha,{\rm cr}}$, i.e., $\hat{L}^{\rm cr} \boldsymbol{e}_n = p_n^{\rm cr} \boldsymbol{e}_n$. Substituting Eq. (31) into Eq. (27) and taking into account the properties of the eigenvectors given in Appendix B, we obtain the following system of equations for the coefficients $F^\ell(t)$ of the expansion (31):

$$\begin{aligned} \frac{dF^\ell}{dt} - F^\ell p_\ell^{\rm cr} &= \frac{1}{2} \left(\frac{dp_\ell}{d \ln R_\alpha} \right)_{\rm cr} \sum_{n=-\infty}^{\infty} F^n(t) \Big[\alpha_n^\ell \\ &+ R_\alpha^2 \, \tilde{\alpha}_n^\ell + \left[R_\alpha^2 - (R_\alpha^{\rm cr})^2 \right] \, G_n^\ell \Big], \end{aligned} \tag{32}$$

where $p_\ell^{\rm cr} = p_\ell(R_\alpha = R_\alpha^{\rm cr})$, and functions α_n^ℓ, $\tilde{\alpha}_n^\ell$ and G_n^ℓ are defined by Eqs. (B1)–(B3) in Appendix B.

The coefficients $F^\ell(t)$ depend on the nonlinearity characterised by α_n^ℓ. The equation for α_n^ℓ is derived from Eq. (30):

$$\begin{aligned} \frac{d\alpha_n^\ell}{dt} + \frac{\alpha_n^\ell}{T_\alpha} &= -2 \sum_{k,s=-\infty}^{\infty} F^k(t) \Big\{ \frac{dF^s}{dt} S_{ksn}^\ell - F^s \Big[M_{ksn}^\ell \\ &- R_\alpha^2 \left(\frac{\alpha_n^\ell}{t_\chi} + K_n^\ell \right) (\overline{\boldsymbol{b}}_p)_k (\overline{\boldsymbol{b}}_p)_s \Big] \Big\} - 2\kappa_{_T} \left(C_1 \alpha_n^\ell - \tilde{\alpha}_n^\ell \right), \end{aligned} \tag{33}$$

where $(\overline{\boldsymbol{b}}_p)_n = {\rm rot}\,(a_n \, \boldsymbol{e}_\varphi)$, and the tensors M_{ksn}^ℓ, S_{ksn}^ℓ, and K_n^ℓ are determined by Eq. (B5)–(B8) in Appendix A. The equation for $\tilde{\alpha}_n^\ell$ is derived from Eq. (30) as well:

$$\begin{aligned} \frac{d\tilde{\alpha}_n^\ell}{dt} + \frac{\tilde{\alpha}_n^\ell}{T_\alpha} &= -2 \sum_{k,s=-\infty}^{\infty} F^k(t) \Big\{ \frac{dF^s}{dt} \tilde{S}_{ksn}^\ell - F^s \Big[\tilde{M}_{ksn}^\ell \\ &- R_\alpha^2 \left(\frac{\tilde{\alpha}_n^\ell}{\tilde{t}_\chi} + \tilde{K}_n^\ell \right) (\overline{\boldsymbol{b}}_p)_k (\overline{\boldsymbol{b}}_p)_s \Big] \Big\} - \kappa_{_T} C_2 \tilde{\alpha}_n^\ell, \end{aligned} \tag{34}$$

where the functions $\tilde{M}_{ksn}^\ell$, $\tilde{S}_{ksn}^\ell$, $\tilde{K}_n^\ell$ are determined by Eq. (B9)–(B11) in Appendix B. It is assumed here that the relaxation time T_α of the magnetic helicity is independent of $\mathbf{r}$. Thus the problem reduces to the study of this infinite system of equations with coefficients determined by the eigenfunctions and eigenvalues of the linear problem for $R_\alpha = R_\alpha^{\rm cr}$. When R_α in the stellar convective zone is not much larger than the critical value $R_\alpha^{\rm cr}$ required for the excitation of the dynamo instability, only a few modes are expected to be excited.

Let us consider the simplest case, when only one mode is excited. This is sufficient to estimate the magnitude of the mean magnetic field in a steady state. The multi-mode regime could be considered similarly. The equations of the single-mode approximation follow from Eqs. (32)–(34):

$$\frac{dF}{dt} - F p^{\rm cr} = F(t) \Big[\left[R_\alpha^2 - (R_\alpha^{\rm cr})^2 \right] \, G + \alpha + R_\alpha^2 \, \tilde{\alpha} \Big], \tag{35}$$

$$\begin{aligned} \frac{d\alpha}{dt} + \frac{\alpha}{T_\alpha} + \kappa_{_T} \left(C_1 \alpha - \tilde{\alpha} \right) &= - \frac{1}{2} \frac{dF^2}{dt} S \\ &+ F^2 \Big[M - R_\alpha^2 \left(K + \frac{\alpha}{t_\chi} \, \overline{\boldsymbol{b}}_p^{\,2} \right) \Big], \end{aligned} \tag{36}$$

$$\begin{aligned} \frac{d\tilde{\alpha}}{dt} + \frac{\tilde{\alpha}}{T_\alpha} + \kappa_{_T} C_2 \tilde{\alpha} &= F^2 \Big[\tilde{M} - R_\alpha^2 \left(\tilde{K} + \frac{\tilde{\alpha}}{\tilde{t}_\chi} \, \overline{\boldsymbol{b}}_p^{\,2} \right) \Big] \\ &- \frac{1}{2} \frac{dF^2}{dt} \tilde{S}, \end{aligned} \tag{37}$$

The steady-state solution of Eqs. (35)–(37) for this single-mode approximation yields the magnitude of the mean toroidal magnetic field near the stellar surface as

$$\overline{B} = (2\pi \overline{\rho}_*)^{1/2} \, \frac{3\eta_{_T} \, \kappa_{_T}}{R_*} \, \left(\frac{2G \, T_\alpha}{K} \right)^{1/2} \, f \left[\frac{R_\alpha^2}{(R_\alpha^{\rm cr})^2} \right], \tag{38}$$

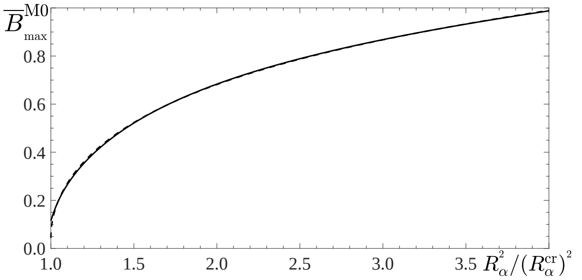

Figure 15. The maximum mean magnetic field $\overline{B}^{\rm M0}_{\rm max}$ versus $(R^2_\alpha/R^{\rm cr}_\alpha)^2$ for the main sequence stars of the spectral class M0, obtained from numerical simulations (solid) of the nonlinear α^2 mean-field dynamo and analytical result (dashed) described by Eqs. (38) and (39).

where

$$f(X) = \left(\frac{X-1}{X-C}\right)^{1/2} \, \left[(R^{\rm cr}_\alpha)^2 X + 2\right]^{-1} \times\left[1 - 2G \, \frac{(R^{\rm cr}_\alpha)^2 X (X-1)}{(X-C) \, [(R^{\rm cr}_\alpha)^2 X + 2]} \, \frac{\overline{\boldsymbol{b}}_p^2}{t_\chi} + \left(1 - 4G \, \frac{(R^{\rm cr}_\alpha)^2 X (X-1)}{(X-C) \, [(R^{\rm cr}_\alpha)^2 X + 2]} \, \frac{\overline{\boldsymbol{b}}_p^2}{t_\chi}\right)^{1/2}\right]^{-1/2}, \quad (39)$$

and we consider the case when $K \approx \tilde{K}$, $M \approx \tilde{M}$, $K/M = C$, $t_\chi \approx \tilde{t}_\chi$ and $C_1 = C_2 = 1$. The characteristic times t_χ and $\tilde{t}_\chi$ are defined by Eqs. (B8) and (B12) in Appendix B.

In Fig. 15 we show the maximum mean magnetic field $\overline{B}^{\rm M0}_{\rm max}$ (solid) versus $(R^2_\alpha/R^{\rm cr}_\alpha)^2$ for the main sequence stars of the spectral class M0 obtained from the mean-field numerical simulations, that is in an agreement with analytical result (dashed) described by Eqs. (38) and (39).

5 CONCLUSIONS

Standard theories of stellar magnetic activity are usually based on the mean-field $\alpha\Omega$ dynamo. However, a majority of the observed stars are fast rotating, because much more easy to observe fast rotating stars generated strong magnetic fields. Our theoretical study and mean-field numerical simulations suggest that for fast rotating low-mass main sequences stars with the spectral classes from M5 to G5, the generated large-scale magnetic field is caused by the mean-field $\alpha^2\Omega$ dynamo, where the α^2 dynamo is modified by a weak differential rotation. However, even weak differential rotation in nonlinear phase of magnetic evolution causes drastic changes in magnetic activity, resulting in chaotic behaviour where long-term evolution (with the period about thousand years) is accompanied by fast changes of the several tens years.

In view of observations, this multi-timescale system causes very complicated patters in magnetic activity, e.g., the stars with the same rotation rates and the same spectral classes may have different magnetic activity. This implies necessity of a long-term programs of observations of the stellar magnetic activity. The long-term behaviour is related to the characteristic time of the evolution of the magnetic helicity density of the small-scale magnetic field. Note also our mean-field numerical simulations have shown that the kinematic and nonlinear phases of magnetic field evolution are very different. For instance, nonlinear effects cause a threshold in the differential rotation that is necessary for a transition between aperiodic and quasi-periodic regime. We demonstrate that period of quasi-periodic oscillations decreases with increase of the differential rotation.

ACKNOWLEDGMENTS

This work was partially supported by the Russian Science Foundation (grant 21-72-20067). We acknowledge the hospitality of NORDITA.

REFERENCES

Baker N., Temesvary S., 1966, Tables of Convective Stellar Envelope Models, New York

Blackman E. G., Field G. B., 2000, Astrophys. J., 534, 984

Bice C. P., Toomre J., 2022, ApJ, 928, 51

Bochanski J. J., Hawley S. L., Covey K. R., West A. A., Reid I. N., Golimowski D. A., Ivezic Z., 2010, Astron. J., 139, 2679

Bondar' N. I., Katsova M. M., Livshits M. A., 2019, Geomagnetism and Aeronomy, 59, 832.

Brandenburg A., Gressel O., Käpylä P. J., Kleeorin N., Mantere M. J. and Rogachevskii I., , 2013, ApJ, 762, 127

Brandenburg A., Kemel K., Kleeorin N., Mitra D., Rogachevskii I., 2011, ApJ, 740, L50

Brandenburg A., Rogachevskii I., Kleeorin N., New J. Phys., 18, 125011

Brandenburg A., Subramanian K., 2005, Phys. Rep., 417, 1

Brown B. P., Oishi J. S., Vasil G. M., et al., 2020, ApJ, 902, L3

Browning M. K., 2008, ApJ, 676, 1262

Bukai M., Eidelman A., Elperin T., Kleeorin N., Rogachevskii I. and Sapir-Katiraie I., 2009, Phys. Rev. E 79, 066302

Chabrier G., Küker M., 2006, A&A, 446,1027

Cox, J. P., Giuli, R. T., 1968, Principles of Stellar Structure. Gordon & Breach, NewYork

Dobler W., Stix M., Brandenburg A., 2006, ApJ, 638, 336

Donati J.-F., Collier Cameron A., Semel M., Hussain G.A.J., Petit P., Carter B.D., Marsden S.C., Mengel M., Lopez Ariste A., Jeffers S. V., Rees D. E., 2003, MNRAS 345, 1145; 1187

Donati J.-F., Morin J., Petit P., Delfosse X., 2008, MNRAS, 390, 545

Elperin T., Kleeorin N., Rogachevskii I., Zilitinkevich S., 2002, Phys. Rev. E, 66, 066305

Elperin T., Kleeorin N., Rogachevskii I., Zilitinkevich S., 2006, Boundary-Layer Meteorol., 119, 449

Field G. B., Blackman E. G., Chou H., 1999, Astrophys. J., 513, 638

Frisch U., Pouquet, A., Leorat, I., Mazure, A. 1975, J. Fluid Mech., 68, 769

Gastine T., Duarte L., Wicht J. 2012. A&A 546, A19.

Gershberg R. E., Kleeorin N., Pustilnik L. A., Shlapnikov, A. A., 2020, Physics of Middle- and Low-Mass Stars with Solar Activity Type, Nauka, Moscow

Gruzinov A. V., Diamond P. H., 1994, Phys. Rev. Lett., 72, 1651

Hawley S. L., Davenport J. R. A., Kowalski A. F., Wisniewski J. P., Hebb L., Deitrick R., Hilton E. J., 2014, ApJ, 797, 121

Henyey, L. G., Vardya, M. S., Bodenheimer, P. 1965, ApJ, 142, 841

Käpylä P. J., 2021, A &A, 65, A66.

Käpylä P. J., Browning, M. K., Brun, A. S. Guerrero, G. Warnecke, J., 2023, e-print ArXiv: 2305.16790.

Kitchatinov L. L., Moss D., Sokoloff D., 2014, Magnetic fields in fully convective M-dwarfs: oscillatory dynamos versus bistability, MNRAS, 442, L1

Kitchatinov L. L., Olemskoy S. V., 2011, MNRAS, 411, 1059

Kleeorin N., Rogachevskii I., 1994, Phys. Rev. E, 50, 2716

Kleeorin N., Rogachevskii I., 1999, Phys. Rev. E, 59, 6724

Kleeorin N., Rogachevskii I., 2003, Phys. Rev. E, 67, 026321

Kleeorin N., Kuzanyan K., Moss D., Rogachevskii I., Sokoloff D., Zhang H., 2003a, A&A, 409, 1097

Kleeorin N., Mond M., Rogachevskii I., 1996, A&A, 307, 293

Kleeorin N., Moss D., Rogachevskii I., Sokoloff D., 2000, A&A, 361, L5

Kleeorin N., Moss D., Rogachevskii I., Sokoloff D., 2002, A&A, 387, 453

Kleeorin N., Moss D., Rogachevskii I., Sokoloff D., 2003b, A&A, 400, 9

Kleeorin N., Rogachevskii I., Ruzmaikin A. A., 1989, Sov. Astron. Lett., 15, 274

Kleeorin N., Rogachevskii I., Ruzmaikin A. A., 1990, Sov. Phys. JETP, 70, 878

Kleeorin N., Rogachevskii I., Ruzmaikin A., 1995, A&A, 297, 159

Kleeorin N., Ruzmaikin A., 1982, Magnetohydrodynamics, 18, 116. Translation from Magnitnaya Gidrodinamika, 2, 17

Kleeorin Y., Safiullin N., Kleeorin N., Porshnev S., Rogachevskii I., Sokoloff D., 2016, MNRAS, 460, 3960

Kleeorin N., Safiullin N., Kuzanyan K. M., Rogachevskii I., Tlatov A., Porshnev S., 2020, MNRAS, 495, 238

Kochukhov O., 2021, A&A Rev., 29, 1

Kochukhov O., Hachman T., Lehtinen J. J., Wehrhahn A., 2020, A&A, 635, A142

Krause F., Rädler K.-H., 1980, Mean-Field Magnetohydrodynamics and Dynamo Theory. Pergamon, Oxford

Moffatt H. K., 1978, Magnetic Field Generation in Electrically Conducting Fluids. Cambridge University Press, New York

Moffatt H. K., Dormy E., 2019, Self-Exciting Fluid Dynamos. Cambridge University Press, Cambridge

Morin J., Donati J.-F., Petit P., Delfosse X., et al., 2010, MNRAS, 407, 2269

Newton E. R., Irwin J., Charbonneau D., Berlind P., Calkins M. L., Mink J., 2017, ApJ, 834, 85

Paxton, B., Bildsten, L., Dotter, A., Herwig F., Lesaffre P. and Timmes, F., 2011, ApJ Suppl. Ser., 192, 3

Parker E., 1979, Cosmical Magnetic Fields. Clarendon, Oxford

Pecaut M. J., Mamajek E. E., 2013, ApJS, 208, 9

Pipin V. V., 2017, MNRAS, 466, 3007

Pipin V. V., Yokoi N., 2018, ApJ, 859, 18

Pouquet A., Frisch U., Leorat J., 1976, J. Fluid Mech., 77, 321

Reiners A., Basri G., 2007, Astrophys.J., 656, 1121

Rogachevskii I., 2021, Introduction to Turbulent Transport of Particles, Temperature and Magnetic Fields. Cambridge University Press, Cambridge

Rogachevskii I., Kleeorin N., 2000, Phys. Rev. E, 61, 5202

Rogachevskii I., Kleeorin N., 2001, Phys. Rev. E., 64, 056307

Rogachevskii I., Kleeorin N., 2004, Phys. Rev. E, 70, 046310

Rogachevskii I., Kleeorin N., 2007, Phys. Rev. E, 76, 056307

Rüdiger G., Hollerbach R., Kitchatinov L. L., 2013, Magnetic Processes in Astrophysics: Theory, Simulations, Experiments. John Wiley & Sons, Weinheim

Ruzmaikin A., Shukurov A. M., Sokoloff D. D., 1988, Magnetic Fields of Galaxies. Kluwer Academic, Dordrecht

Saar S. H., 1996, In: Uchida Y., Kosugi T., Hudson H. S., (eds) Magnetodynamic phenomena in the solar atmosphere. IAU colloquium, vol 153. Kluwer, Dordrecht

Saar S. H., Linsky J. L., 1985, Astrophys.J., 299, L47

Safiullin N., Kleeorin N., Porshnev S., Rogachevskii I., Ruzmaikin A., 2018, J. Plasma Phys. 84, 735840306

Schrinner M., Petitdemange L., Dormy E. 2012, ApJ, 752, 121

Shukurov A., Subramanian K., 2021, Astrophysical Magnetic Fields: From Galaxies to the Early Universe. Cambridge University Press, Cambridge

Shulyak D., Sokoloff D., Kitchatinov L., Moss D., 2015, MNRAS, 449, 3471

Spruit H. C., 1974, Solar Phys., 34, 277

Strassmeier K. G., 2009, Astron. Astrophys. Rev., 17, 251

Warnecke J., Losada I. R., Brandenburg A., Kleeorin N., Rogachevskii I., 2013, ApJ, 777, L37

Winters J. G., Henry T. J., Jao W. C., Subasavage J. P., Chatelain J. P., Slatten K., Riedel A. R., Silverstein M. L., Payne M. J., 2019, Astron. J., 157, 216

Wright N. J., Newton E. R., Williams P. K. G., Drake J. J., Yadav R. K., 2018, MNRAS, 479, 2351

Yadav R. K., Christensen U. R., Morin J., et al. 2015, ApJ, 813, L31

Yadav R. K., Christensen U. R., Wolk S. J., et al., 2016, ApJ, 833, L28

Zeldovich Ya. B., Ruzmaikin A. A., Sokoloff, D. D., 1983, Magnetic Fields in Astrophysics, Gordon and Breach, New York

Zhang H., Sokoloff D., Rogachevskii I., Moss D., Lamburt V., Kuzanyan K., Kleeorin N., 2006, MNRAS, 365, 276

Zhang H., Moss D., Kleeorin N., Kuzanyan K., Rogachevskii I., Sokoloff D., Gao Y., Xu H., ApJ, 2012, 751, 47

APPENDIX A: THE FUNCTIONS $\Psi_1(\omega)$ AND $\Psi_2(\omega)$

The functions $\Psi_1(\omega)$ and $\Psi_2(\omega)$ are given by

$$\begin{aligned}\Psi_1(\omega) = (3-\sigma)\Big[4A_1^{(3)}(2\omega) - \frac{3}{\pi}\bar{A}_1(\omega^2)\Big] - \frac{\lambda}{2}\Big[4A_1^{(2)}(2\omega) \\ -A_1^{(2)}(\omega)\Big] + 3(\sigma-1)\Big[4C_1^{(3)}(2\omega) - \frac{3}{\pi}\bar{C}_1(\omega^2)\Big],\end{aligned}$$

$$\Psi_2(\omega) \quad = \quad 3(\sigma-1)\left[4C_3^{(3)}(2\omega) - \frac{3}{\pi}\bar{C}_3(\omega^2)\right].$$

where

$$\begin{aligned}A_1^{(2)}(\omega) &= 6\Big[\frac{\arctan(\omega)}{\omega}\Big(1+\frac{1}{\omega^2}\Big) - \frac{3}{\omega^2} + \frac{2}{\omega^3}S(\omega)\Big],\\ A_1^{(3)}(\omega) &= J_0^{(3)}(\omega) - J_2^{(3)}(\omega),\\ C_1^{(3)}(\omega) &= \frac{1}{4}\Big[J_0^{(3)}(\omega) - 2J_2^{(3)}(\omega) + J_4^{(3)}(\omega)\Big],\\ C_3^{(3)}(\omega) &= \frac{1}{4}\Big[-J_0^{(3)}(\omega) + 6J_2^{(3)}(\omega) - 5J_4^{(3)}(\omega)\Big],\end{aligned}$$

and

$$\bar{A}_1(\omega^2) = \frac{2\pi}{\omega^2}\Big[(\omega^2+1)\frac{\arctan(\omega)}{\omega} - 1\Big],$$

$$\bar{C}_1(\omega^2) = \frac{\pi}{2\omega^4}\Big[(\omega^2+1)^2\frac{\arctan(\omega)}{\omega} - \frac{5\omega^2}{3} - 1\Big],$$

$$\bar{C}_3(\omega^2) = -\frac{\pi}{2\omega^4}\left[\left[\omega^4+6\omega^2+5\right]\frac{\arctan(\omega)}{\omega} - \frac{13\omega^2}{3} - 5\right].$$

where

$$\begin{aligned}J_0^{(3)}(\omega) &= 2\Big[2\frac{\arctan(\omega)}{\omega} + \frac{1}{\omega^4}\ln\left(1+\omega^2\right) - \frac{1}{\omega^2}\Big],\\ J_2^{(3)}(\omega) &= \frac{6}{\omega^2}\Big[1 - 2\frac{\arctan(\omega)}{\omega} + \frac{1}{\omega^2}\ln\left(1+\omega^2\right)\Big],\end{aligned}$$

$$\begin{aligned}J_4^{(3)}(\omega) = \frac{2}{\omega^2}\Big[1 - \frac{3}{\omega^2}\Big(2\frac{\arctan(\omega)}{\omega} - 2 \\ +\ln\left(1+\omega^2\right)\Big)\Big],\end{aligned}$$

and $S(\omega) = \int_0^\omega [\arctan(y)/y]\,dy$.

In the case of $\omega \ll 1$ these functions are given by

$$A_1^{(2)}(\omega) = \frac{8}{3}\left(1 - \frac{3\omega^2}{25}\right),$$

$$A_1^{(3)}(\omega) = 2\left(1 - \frac{2\omega^2}{15}\right),$$

$$C_1^{(3)}(\omega) = \frac{2}{5}\left(1 - \frac{2\omega^2}{21}\right), \quad C_3^{(3)}(\omega) = -\frac{8}{105}\,\omega^2,$$

$$J_0^{(3)}(\omega) = 3\left(1 - \frac{2\omega^2}{9} + \frac{\omega^4}{10}\right),$$

$$J_2^{(3)}(\omega) = 1 - \frac{2\omega^2}{5} + \frac{3\omega^4}{14},$$

$$J_4^{(3)}(\omega) = \frac{3}{5}\left(1 - \frac{10\omega^2}{21} + \frac{5\omega^4}{18}\right),$$

In the case of $\omega \gg 1$ these functions are given by

$$A_1^{(2)}(\omega) = \frac{3\pi}{\omega} - \frac{24}{\omega^2}, \quad A_1^{(3)}(\omega) = \frac{2\pi}{\omega},$$

$$C_1^{(3)}(\omega) = \frac{\pi}{2\omega}, \quad C_3^{(3)}(\omega) = -\frac{\pi}{2\omega},$$

$$J_0^{(3)}(\omega) = \frac{2\pi}{\omega} - \frac{6}{\omega^2},$$

$$J_2^{(3)}(\omega) = \frac{6}{\omega^2}, \quad J_4^{(3)}(\omega) = \frac{2}{\omega^2}.$$

In the case of $\omega^2 \ll 1$ these functions are given by

$$\begin{aligned}\bar{A}_1(\omega^2) &\sim \frac{4\pi}{3}\left(1 - \frac{\omega^2}{5}\right), \quad \bar{A}_2(\omega^2) \sim -\frac{8\pi}{15}\,\omega^2,\\ \bar{C}_1(\omega^2) &\sim \frac{4\pi}{15}\left(1 - \frac{\omega^2}{7}\right), \quad \bar{C}_2(\omega^2) \sim \frac{32\pi}{315}\,\omega^4,\\ \bar{C}_3(\omega^2) &\sim -\frac{8\pi}{105}\,\omega^2.\end{aligned}$$

In the case of $\omega^2 \gg 1$ these functions are given by

$$\begin{aligned}\bar{A}_1(\omega^2) &\sim \frac{\pi^2}{\omega}, \quad \bar{A}_2(\omega^2) \sim -\frac{\pi^2}{\omega},\\ \bar{C}_1(\omega^2) &\sim \frac{\pi^2}{4\omega} - \frac{4\pi}{3\omega^2}, \quad \bar{C}_2(\omega^2) \sim \frac{3\pi^2}{4\omega},\\ \bar{C}_3(\omega^2) &\sim -\frac{\pi^2}{4\omega} + \frac{8\pi}{3\omega^2}.\end{aligned}$$

APPENDIX B: FUNCTIONS FOR AXI-SYMMETRIC NONLINEAR α^2 DYNAMO

The functions α_n^ℓ, $\tilde{\alpha}_n^\ell$ and G_n^ℓ entering in Eq. (32), are given by

$$\alpha_n^\ell = Q_\ell^{-1}\int \alpha_{\rm m}\, a^{\ell,*}\, b_n\, d^3r, \tag{B1}$$

$$\tilde{\alpha}_n^\ell = Q_\ell^{-1}\int \alpha_{\rm m}\, \hat{M}(b^{\ell,*}, a_n)\, d^3r, \tag{B2}$$

$$G_n^\ell = Q_\ell^{-1}\int \alpha_{\rm k}\, \hat{M}(b^{\ell,*}, a_n)\, d^3r, \tag{B3}$$

$$Q_\ell = \int \alpha_{\rm k}\, a^{\ell,*}\, b_\ell\, d^3r. \tag{B4}$$

The tensors M_{ksn}^ℓ, S_{ksn}^ℓ, and K_n^ℓ entering in Eq. (33) are given by

$$M_{ksn}^\ell = Q_\ell^{-1}\int \frac{\hat{M}(b_k, a_s)}{\rho(r)}\, a^{\ell,*}\, b_n\, d^3r, \tag{B5}$$

$$S_{ksn}^\ell = Q_\ell^{-1}\int \frac{1}{\rho(r)}\, a^{\ell,*}\, b_n b_k a_s\, d^3r, \tag{B6}$$

$$K_n^\ell = Q_\ell^{-1}\int \frac{\alpha_{\rm k}}{\rho(r)}\, a^{\ell,*}\, b_n\, d^3r, \tag{B7}$$

$$t_\chi^{-1} = Q_\ell^{-1}\int a^{\ell,*}\, b_n\, d^3r. \tag{B8}$$

The tensors $\tilde{M}_{ksn}^\ell$, $\tilde{S}_{ksn}^\ell$, $\tilde{K}_n^\ell$ entering in Eq. (34) are given by

$$\tilde{M}^{\ell}_{ksn} = Q_{\ell}^{-1} \int \frac{1}{\rho(r)} \, \hat{M}(b_k, a_s) \, \hat{M}(b^{\ell,*}, a_n) \, d^3 r, \tag{B9}$$

$$\tilde{S}^{\ell}_{ksn} = Q_{\ell}^{-1} \int \frac{1}{\rho(r)} \, \hat{M}(b^{\ell,*}, a_n) \, b_k \, a_s \, d^3 r, \tag{B10}$$

$$\tilde{K}^{\ell}_{n} = Q_{\ell}^{-1} \int \frac{\alpha_{\mathrm{k}}}{\rho(r)} \, \hat{M}(b^{\ell,*}, a_n) \, d^3 r, \tag{B11}$$

$$\tilde{t}_{\chi}^{-1} = Q_{\ell}^{-1} \int \frac{1}{\rho(r)} \, \hat{M}(b^{\ell,*}, a_n) \, d^3 r. \tag{B12}$$